# Temperature and magnetic field dependent Raman study of electron-phonon interactions in thin films of Bi<sub>2</sub>Se<sub>3</sub> and Bi<sub>2</sub>Te<sub>3</sub> nanoflakes

Sören Buchenau , 1,\* Sarah Scheitz, Astha Sethi, John E. Slimak, Tomke Eva Glier, Pranab Kumar Das, Torben Dankwort, Lewis Akinsinde, Lorenz Kienle, Andrivo Rusydi, Clemens Ulrich, S. Lance Cooper, and Michael Rübhausen

<sup>1</sup>CFEL, University Hamburg, Luruper Chaussee 175, 22761 Hamburg, Germany

<sup>2</sup>Department of Physics and Materials Research Laboratory, University of Illinois, Urbana, Illinois 61801, USA

<sup>3</sup>Singapore Synchrotron Light Source, National University of Singapore, Singapore 117603, Singapore

<sup>4</sup>Institute for Materials Science, Kiel University, Kaiserstrasse 2, 24143 Kiel, Germany

<sup>5</sup>School of Physics, The University of New South Wales, New South Wales 2052, Sydney, Australia



(Received 8 October 2019; accepted 26 May 2020; published 22 June 2020)

We have investigated two-dimensional nanostructures of the topological insulators  $Bi_2Se_3$  and  $Bi_2Te_3$  by means of temperature and magnetic field dependent Raman spectroscopy. The surface contribution of our samples was increased by using thin films of dropcasted nanoflakes with the aim of enhancing their topological properties. Raman spectroscopy provides a contact-free method to investigate the behavior of topological properties with temperature and magnetic fields at lower dimensions. The temperature dependent Raman study reveals anharmonic phonon behavior for  $Bi_2Te_3$  indicative of a two-phonon relaxation mechanism in this material. Contrary to this,  $Bi_2Se_3$  shows clear deviations from a two-phonon anharmonic decay model at temperatures below 120 K exhibiting a hardening and broadening, especially of the  $A_{1g}^2$  mode. Similarly, the magnetic field dependent self-energy effects are only observed for the  $A_{1g}^2$  mode of  $Bi_2Se_3$ , showing a broadening and hardening with increasing field. We interpret our results in terms of corrections to the phonon self-energy for  $Bi_2Se_3$  at temperatures below 120 K and magnetic fields above 4 T due to electron-hole pair excitations associated with the conducting surface states. The phonon renormalization with increasing magnetic field is explained by a gap opening in the Dirac cone that enables phonon coupling to the changing electric susceptibility.

## DOI: 10.1103/PhysRevB.101.245431

## I. INTRODUCTION

Topological insulators (TIs) are a new class of materials, which are insulating in the bulk and host conducting surface states (CSSs) at the interface between the TI and conventional insulators [1]. The idea of topological states was strongly promoted during the aftermath of the discovery of the quantum Hall effect by von Klitzing [2], who identified specific quantized changes in the Hall conductance, which turn out to be topological quantum numbers. After several incremental steps, modern three-dimensional (3D) TIs were predicted in 2007 by Fu et al. [3]. The strong spin-orbit coupling leads, in specific materials, to a band inversion of two p bands [4], which is essential for the CSSs. In addition, the electron transport is characterized by spin-momentum locking and a linear dispersion relation, known as a Dirac cone, superimposed on the bulk bands [5].  $Bi_2X_3$  (X=Se, Te) belongs to the most frequently studied 3D TI with a single Dirac cone at the  $\Gamma$ point of the Brillouin zone [6,7] and bulk band gaps of 0.3 eV [8] and 0.1 eV [9] for Bi<sub>2</sub>Se<sub>3</sub> and Bi<sub>2</sub>Te<sub>3</sub>, respectively.

To explicitly study the CSSs and reduce contributions from the bulk, we have examined dropcasted nanoflakes with high aspect ratios that lead to an increased surface contribution.

In order to evaluate the fundamental limit of the conductivity of electrons in the CSSs at lower dimensions, it is

\*Corresponding author: sbuchena@physnet.uni-hamburg.de

important to study the electron-phonon interactions of these 2D materials [10,11].

A unique technique to study phononic and electronic properties of solids simultaneously is Raman scattering, which has been widely applied to investigate bulk samples and conventional 2D films of Bi<sub>2</sub>Se<sub>3</sub> [12–15] and Bi<sub>2</sub>Te<sub>3</sub> [14,16,17]. Bi<sub>2</sub>Se<sub>3</sub> and Bi<sub>2</sub>Te<sub>3</sub> are layered materials with a rhombohedral crystal structure that grow in multiples of so-called quintuple layers (QLs) consisting of alternating Bi and Se or Te layers, as depicted in Fig. 1(a) [18]. The primitive unit cell consists of five atoms, which results in 15 lattice dynamical modes that are classified in three acoustic and 12 optical modes. The optical modes are further grouped into four Raman-active modes with two modes each of  $A_{1g}$  and  $E_{\rm g}$  symmetry and four infrared(IR)-active modes with two modes each of  $A_{1u}$  and  $E_{u}$  symmetry according to group theory [18]. Due to the inversion symmetry of the crystal structure, these phonon modes are exclusively either Raman or IR active [18]. Of the Raman-active phonons, the  $A_{1g}$  modes are out-of-plane vibrations, whereas the  $E_g$  modes vibrate in-plane.

Systematic temperature dependent Raman studies have been conducted before on  $Bi_2Se_3$  single crystals [19,20] and nanoplates [21], and on  $Bi_2Te_3$  thin films [22]. In this work, we report on a temperature and magnetic field dependent high-energy-resolution Raman study of thin films of individual  $Bi_2Se_3$  and  $Bi_2Te_3$  nanoflakes with average heights in the range of 8 and 14 QLs, respectively.

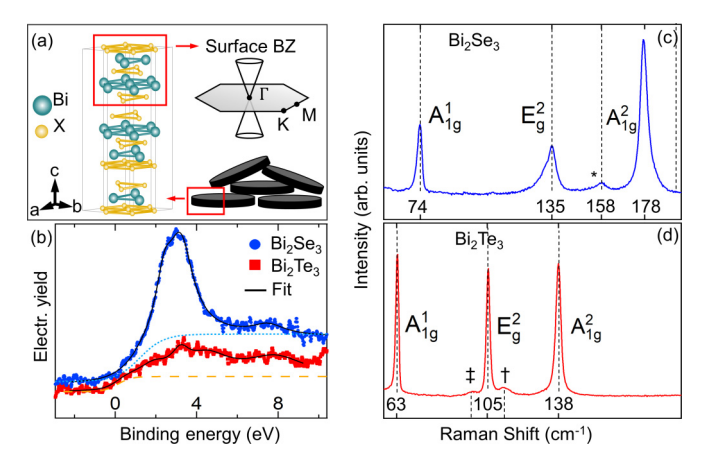


FIG. 1. (a) Schematic illustration of a thin film of  $\text{Bi}_2X_3$  (X=Se, Te) nanoflakes. This configuration greatly enhances the amount of surface, which hosts massless Dirac electrons due to the linear Dirac cone at the  $\Gamma$  point [29], as shown in the surface Brillouin zone in the upper right corner. The figure further shows the crystal structure with blue spheres representing Bi atoms and yellow spheres representing either Se or Te atoms. (b) Valence-band emission spectra extracted from XPS spectra of both materials. The Fermi edge modeled by a step function shows a highly increased electron density for  $\text{Bi}_2\text{Se}_3$  (light-blue, dotted graph) compared to  $\text{Bi}_2\text{Te}_3$  (orange, dashed graph). (c),(d) Raman spectra at 3 K in  $z(xx)\overline{z}$  geometry showing three labeled bulk modes for  $\text{Bi}_2\text{Se}_3$  and  $\text{Bi}_2\text{Te}_3$ , respectively. The asterisk, dagger, and double dagger mark Ramanforbidden infrared modes.

Magnetic field dependent Raman measurements are of utmost importance as they allow for investigations of the destruction of the CSSs by gapping of the Dirac cone induced by the presence of a magnetic field [1]. It was theoretically predicted that the CSSs are sensitive to the application of a magnetic field [23] and an opening of the Dirac cone has indeed been observed in magnetically doped TIs [24,25] or by exchange coupling TIs to magnetic insulators [26–28]. The tuning of the CSSs with an applied magnetic field is expected to display a spectroscopic signature, which is amplified due to the highly increased surface contributions of our nanoflakes. We therefore interpret our results by means of self-energy corrections of the phonons due to electron-phonon interactions.

## II. EXPERIMENTAL PART

Figure 1(a) shows an illustration of strongly anisotropic nanoflakes. The Bi<sub>2</sub>Se<sub>3</sub> nanoflakes were grown with the chemical polyol method following our earlier work [30]. The Bi<sub>2</sub>Te<sub>3</sub> nanoflakes were synthesized using a slightly modified route according to Zhang *et al.* [31]. Details on the synthesis are presented in Ref. [30] and in the Supplemental Material [32]. The clean flakes were dropcasted on a Si substrate and the solvent evaporated. It should be noted that the structures are not damaged by these preparatory steps, as can be seen in Fig. S-2 of the Supplemental Material [32]. The required stoichiometry, single crystallinity, and morphology of both samples were confirmed using energy dispersive x-ray spectroscopy (EDX), x-ray photoelectron spectroscopy (XPS), transmission electron microscopy (TEM), selected area electron diffraction (SAED), and atomic

force microscopy (AFM). A detailed characterization of the nanoflakes can be found in the Supplemental Material [32].

The topological insulator  $Bi_2X_3$  (X=Se, Te) features Dirac states at the interface with conventional insulators, but not at the interface of every QL [28]. It has furthermore been shown for Bi<sub>2</sub>Se<sub>3</sub>, that the CSS wave functions hybridize below a critical flake thickness of 6 QLs, which results in a gap opening in the Dirac cone [33]. To investigate the intact CSSs, it is hence necessary to grow flakes of certain thicknesses and maintain enough space between dropcasted flakes to prevent hybridization of the CSSs from neighboring flake surfaces. With average heights of 8 and 14 QLs for our Bi<sub>2</sub>Se<sub>3</sub> and Bi<sub>2</sub>Te<sub>3</sub> flakes, respectively, we expect our samples to host unperturbed CSSs. In addition, our flakes were grown covered with the ligand polyvinylpyrrolidone (PVP) to facilitate a 2D growth. The PVP layers act as conventional insulators and thus provide sufficient spacing between neighboring flakes. It is known that the CSSs are robust against different kinds of adsorbates and are maintained even under ambient environmental conditions [24,34]. However, adsorbates are known to induce a band bending of the bulk bands near the surface due to charge accumulation [6,35]. This leads to the creation of additional surface quantum well states originating from the bulk bands coexisting next to the CSSs. Nonetheless, the CSSs stay intact, but are pushed deeper into the bulk separating them from the surface defects [36]. Thus, for volume scattering techniques, the CSSs stay detectable as Raman scattering is able to probe the whole volume including the deeper-lying CSSs, in contrast to surface sensitive techniques such as angle-resolved photoemission spectroscopy (ARPES). In fact, Raman scattering probes the complete thickness of a flake of about 10 nm. Therefore, probing a thin film of dropcasted nanoflakes is expected to contain a manifold of topologically nontrivial contributions, as illustrated in Fig. 1(a), making it easier to observe phenomena that have their origin in those exotic states.

We conducted Raman measurements on films of dropcasted nanoflakes using the 647.1 nm excitation line of a continuous-wave Kr<sup>+</sup> gas laser. The incident laser power was limited to 6.2 mW and focused on a 50-\mu m-diameter spot size to prevent laser induced heating or damage of the sample, which is shown in detail in the Supplemental Material [32]. The sample was mounted so that the incident light impinged on the flakes perpendicular to their surfaces. The scattered light from the sample was collected in a backscattering configuration, dispersed through a triple-stage spectrometer, and then detected with a liquid-nitrogen-cooled charged-coupleddevice detector. The horizontal polarization of the incident light with regard to the setup was selected with a polarization rotator and the scattered light was analyzed by the triplestage gratings of the spectrometer that is primarily sensitive to horizontally polarized light [37]. Our scattering configuration denoted in Porto notation is hence  $z(xx)\overline{z}$  [38]. The samples were inserted into a continuous He-flow cryostat, which itself was horizontally mounted in the open bore of a superconducting magnet. This setup allowed for simultaneous temperature (3-295 K) and magnetic field (0-7 T) dependent measurements. Magnetic field dependent measurements were performed in Faraday geometry with the wave vector of the incident light  $\vec{q}$  parallel to the applied field  $\vec{H}$ .

### III. RESULTS AND DISCUSSION

Figure 1(b) shows the valence-band spectra extracted from XPS measurements of the Bi<sub>2</sub>Se<sub>3</sub> and Bi<sub>2</sub>Te<sub>3</sub> films. The indicated Fermi edges modeled by step functions reveal, for Bi<sub>2</sub>Se<sub>3</sub>, a highly increased electron density near the Fermi edge compared to Bi<sub>2</sub>Te<sub>3</sub>. Differences in the two samples are also reflected in their phononic properties measured by Raman spectroscopy. The implication of the enhanced surface contribution of our flakes is already observable in the representative Raman spectra shown in Figs. 1(c) and 1(d). Next to the three identified bulk phonon modes that are in good agreement with previous experiments [18,39,40], additional IR-active modes at 158 cm<sup>-1</sup> in Bi<sub>2</sub>Se<sub>3</sub> and at 98 cm<sup>-1</sup> and 113 cm<sup>-1</sup> in Bi<sub>2</sub>Te<sub>3</sub> are detected [14,15,41]. The IR-active modes become Raman active because of the breaking of the crystal's inversion symmetry at the surface of the nanoflakes [15]. This aspect is a direct manifestation of the enhanced surface-to-volume ratio of the dropcasted nanoflakes compared to the bulk material. The bulk material crystallizes in the  $D_{3d}$  space group with inversion symmetry, whereas the symmetry at the surface is reduced to  $C_{3v}$  [15]. Gnezdilov *et al.* [15] reported that the  $A_{2v}^2$ mode at 158 cm<sup>-1</sup> in the case of Bi<sub>2</sub>Se<sub>3</sub> is only observable at temperatures below 10 K for their bulk crystalline sample. In contrast, for our nanoflake samples, we were able to observe this mode even at elevated temperatures up to  $\sim 160 \text{ K}$ (see Fig. S-9 in the Supplemental Material [32]), indicating enhanced surface contributions with respect to the scattering volume at lower temperatures. Likewise, the IR modes in the Bi<sub>2</sub>Te<sub>3</sub> films are detected for temperatures up to 100 K (see Fig. S-9 in the Supplemental Material [32]). Furthermore, the high single crystalline quality of our flakes is indicated by the nearly resolution-limited linewidths of the Bi<sub>2</sub>Te<sub>3</sub> phonons. In Sec. 5 in the Supplemental Material [32], we discuss in detail that the narrow linewidths and high quality of the Bi<sub>2</sub>Se<sub>3</sub> spectra suggest nearly stoichiometric samples with only a few Se vacancies. Furthermore, a sensitivity of the phonons to band-bending effects due to adsorbates at the surface and consequent localized electronic surface states cannot be seen. Since Raman is a volume scattering technique, we do not expect to observe any contributions from possible highly localized electronic states at the sample surface. This leads us to conclude that the phonons track the CSSs and electronic states associated to the Fermi level of our sample. Furthermore, we conclude from the low number of Se vacancies that the Fermi level in our sample lies indeed between the bulk valence and conduction band.

We conducted a detailed temperature dependent Raman study by acquiring 30 spectra for each material system in a temperature range from 3 to 295 K. To investigate the phonon dynamics, we extracted the values of the frequency  $\omega$  and the linewidth  $\Gamma$  [full width at half maximum (FWHM)] from the respective Voigt fits to the phonon modes. The Voigt profile is represented by a Lorentz profile broadened by a Gaussian that accounts for the spectral resolution of the spectrometer, and is given as

$$V(\omega) = y_0 + A \frac{2 \ln 2}{\pi^{3/2}} \frac{\Gamma_L}{\Gamma_G^2}$$

$$\times \int_{-\infty}^{\infty} \frac{e^{-t^2}}{\left(\sqrt{\ln 2} \frac{\Gamma_L}{\Gamma_G}\right)^2 + \left(\sqrt{4 \ln 2} \frac{\omega - \omega_0}{\Gamma_G} - t\right)^2} dt. \quad (1)$$

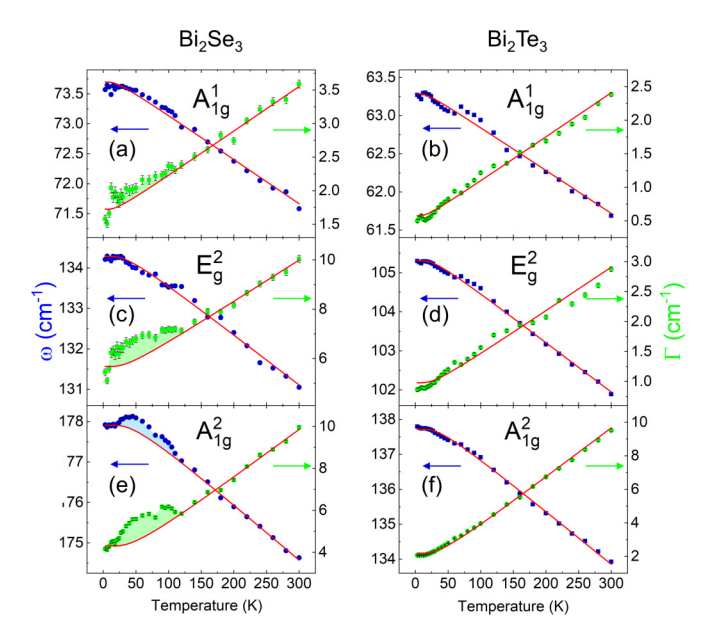


FIG. 2. Self-energy effects from Voigt fits of the temperature dependent Raman response for  $\mathrm{Bi_2Se_3}$  (left column) and  $\mathrm{Bi_2Te_3}$  (right column). (a),(b) The  $A_{\mathrm{Ig}}^1$  phonons, (c),(d) the  $E_{\mathrm{g}}^2$  phonons, and (e),(f) the  $A_{\mathrm{Ig}}^2$  phonons. The red lines are fits using the model of an anharmonic decay with a symmetric decay channel into two acoustic phonons. The data show the general trend of an anharmonic decay consisting of broadening and softening with increasing temperature. Clear deviations from the model are present for the high-energy modes in  $\mathrm{Bi_2Se_3}$  [(c) and (e)], which are mirrored in energy and linewidth. Below  $\sim 120$  K, the phonons exhibit higher energies and linewidths than expected from the usual anharmonic phonon decay, as an indication for additional phonon interactions with the electronic system.

Hereby,  $\Gamma_{G,L}$  denotes the linewidth of both convoluted peaks, with a spectral resolution of the setup of  $\Gamma_G$ =1.4 cm<sup>-1</sup>,  $\omega_0$  is the peak center, A is the integrated area of the Lorentzian peak, and  $y_0$  is the offset.

We have analyzed the three higher-energy modes of the commonly known [14,39] four bulk modes in  $\text{Bi}_2X_3$  (X=Se, Te) because the lowest-energy  $E_{\rm g}^1$  mode was covered by the strong Rayleigh background due to the enhanced elastic scattering from the nanoflakes. Figure 2 shows the behavior of the frequency  $\omega_0$  and linewidth  $\Gamma_{\rm L}$  of the  $A_{\rm lg}^1$ ,  $E_{\rm g}^2$ , and  $A_{\rm lg}^2$  modes for  $\text{Bi}_2\text{Se}_3$  (left column) and  $\text{Bi}_2\text{Te}_3$  (right column). The frequencies and linewidths show a general trend of phonon softening and broadening with increasing temperature by several wave numbers. This phonon behavior can be described by the model of an anharmonic decay (AD) assuming a symmetric decay of the optical phonon into two acoustic phonons [42]. Within this model, the temperature dependences of the phonon frequency and linewidth are given by

$$\omega_{\text{anh}}(T) = \omega_0 - \frac{a}{e^{\frac{\hbar\omega_0}{2J_BT}} - 1},$$
 (2)

$$\Gamma_{\rm anh}(T) = \Gamma_0 + \frac{a}{e^{\frac{\hbar\omega_0}{2E_{\rm B}T}} - 1},\tag{3}$$

with T as the temperature,  $\omega_{anh}$  and  $\Gamma_{anh}$  as the modulated frequency and linewidth, respectively, and  $\omega_0$  and  $\Gamma_0$  as the bare phonon frequency and linewidth of a particular phonon, respectively. a contains the transition matrix element and the two-phonon density of states of the anharmonic decay. Fits of the data according to the AD model are shown as red lines in Fig. 2. For Bi<sub>2</sub>Te<sub>3</sub>, the anharmonic fits show very good agreement with the data, especially for the highest-energy  $A_{1g}^2$  mode in Fig. 2(f). This indicates a more bulklike behavior typical for semiconductors and insulators with phononphonon interactions as the dominant scattering mechanism in the Bi<sub>2</sub>Te<sub>3</sub> sample. Compared to Bi<sub>2</sub>Te<sub>3</sub>, the linewidths for all Raman modes in Bi<sub>2</sub>Se<sub>3</sub> show clear deviations from the AD model at temperatures below 120 K; see Figs. 2(a), 2(c) and 2(e). The linewidth of the  $A_{1g}^1$  mode exhibits only weak deviations from the AD model, whereas the higherenergy modes deviate more strongly. For the  $A_{1g}^2$  mode, the deviation in linewidth is mirrored in frequency, illustrated in Fig. 2(e), as expected by the Kramers-Kronig relation. In previous temperature dependent Raman investigations on Bi<sub>2</sub>Se<sub>3</sub> crystals [19,20], no phonon anomalies were observed. This hints to an origin of these deviations stemming from the increased electronic surface contributions of the investigated flakes at lower temperatures. This aspect is supported by the enhanced electron density near the Fermi edge in Bi<sub>2</sub>Se<sub>3</sub>, shown in Fig. 1(b).

Since the AD model is not sufficient to describe the low-temperature behavior of phonons, additional scattering mechanisms need to be taken into consideration. As Bi<sub>2</sub>Se<sub>3</sub> is nonmagnetic, additional scattering channels could stem from electron-phonon interactions since the only available states at these energies and low temperatures must be of an electronic nature. The coupling of phonons to available electronic susceptibilities would result in a decay of the phonons by creating electron-hole pairs [43,44]. The possibility of this interaction is plausible since our XPS data show a higher electron density near the Fermi edge for Bi<sub>2</sub>Se<sub>3</sub>. The coupling of phonons to an electric susceptibility  $\chi^{el}(\omega)$  leads to a correction in the phonon self-energy, which manifests itself in a modified Raman response. This response  $I^{ph}(\omega)$  of a phonon coupled to an electric susceptibility  $\chi^{el}(\omega)$ ,

$$\chi^{\text{el}}(\omega) = R(\omega) + i\rho(\omega),$$
 (4)

with its real  $R(\omega)$  and imaginary part  $\rho(\omega)$ , is expressed by [45,46]

$$I^{\text{ph}}(\omega) \propto \frac{[g^2 \rho(\omega) + \Gamma_{\text{anh}}] \omega_{\text{anh}}}{\left\{\omega^2 - \underbrace{\omega_{\text{anh}}^2 \left[1 - g^2 \frac{R(\omega)}{\omega_{\text{anh}}}\right]}_{\omega_{\text{exp}}^2}\right\}^2 + \omega_{\text{anh}}^2 \underbrace{\left[\Gamma_{\text{anh}} + g^2 \rho(\omega)\right]^2}_{\Gamma_{\text{exp}}^2}}.$$
(5)

Here,  $\omega_{\rm anh}$  and  $\Gamma_{\rm anh}$  correspond to the frequency and linewidth expected from the AD model, and g is a coupling constant determining the coupling strength between the phonon and the electric susceptibility. Equation (5) describes a Lorentz profile with a phonon frequency  $\omega_{\rm anh}$  that is modified by coupling to the real part  $R(\omega)$  of the electric susceptibility and a linewidth  $\Gamma_{\rm anh}$  modified by coupling to the imaginary part  $\rho(\omega)$ . As a result, the values for the frequency  $\omega_{\rm exp}$  and

linewidth  $\Gamma_{\rm exp}$  extracted from Voigt fits of the phonons differ from the values expected for an anharmonic decay due to corrections from the electric susceptibility. We hence interpret the deviations in linewidth and frequency expected from the AD model as arising from additional contributions caused by the decay of phonons coupling to an available electronic transition. When the electron-phonon coupling g is strong enough, the extracted phonon linewidths and frequencies are therefore given as follows:

$$\omega_{\rm exp} = \sqrt{\omega_{\rm anh}(T)^2 - \omega_{\rm anh}(T) \cdot g^2 R(\omega)},\tag{6}$$

$$\Gamma_{\rm exp} = \Gamma_{\rm anh}(T) + g^2 \rho(\omega).$$
 (7)

The deviations from the AD model could be caused by an interaction of the phonons with an electric susceptibility with an energy in the meV range. The lack of any electronic renormalization in  $Bi_2Te_3$  is thus indicating that there are no available electronic states in this energy range. This is further verified by the strongly diminished electronic density near the Fermi edge in  $Bi_2Te_3$  compared to  $Bi_2Se_3$  seen by XPS, as shown in Fig. 1(b).

Since the  $A_{1g}^2$ - and  $E_g^2$ -symmetry phonons show deviations from the AD model, it can be argued that both phonons couple to a close-lying electronic transition. The different energies of the two phonons lead to different corrections from the real and imaginary parts of the electric susceptibility according to Eqs. (6) and (7).

The strong electronic renormalization in Bi<sub>2</sub>Se<sub>3</sub> for the  $E_{\sigma}^2$ mode in linewidth but none in frequency, shown in Fig. 2(c), leads to the assumption that the  $E_{\rm g}^2$  phonon couples to an electric susceptibility with an energy identical to the  $E_{\rm g}^2$ energy, as visualized in Fig. 3(a). In that way, the  $E_g^2$  phonon would get a strong correction from the imaginary part  $\rho(\omega)$ since it is located at the maximum, resulting in an increased linewidth  $\Gamma_{exp}$  according to Eq. (7). On the other hand, there would not be any corrections in frequency because at  $\omega_{\rm ph}$ the real part  $R(\omega)$  is zero and thus  $\omega_{\rm exp}$  corresponds to  $\omega_{\rm anh}$ according to Eq. (6). The temperature dependence of the  $E_{\sigma}^2$ frequency is then sufficiently well described by the AD model,  $\tilde{l}$ , as evident in Fig. 2(c). Following this hypothesis, the  $A_{1g}^2$ phonon with an energy of 22 meV would couple to  $\rho(\omega)$  and  $\ddot{a}$ negative  $R(\omega)$  of the same electric susceptibility, as illustrated in Fig. 3(b). This would again result in increased linewidths and additionally in increased frequencies according to Eqs. (6) and (7). Our hypothesis agrees well with the observed deviations in frequency and linewidth at lower temperatures for the  $A_{10}^2$  phonon shown in Fig. 2(e). In this picture, we expect to observe these effects at lower temperatures where phonons are frozen out and the scattering mechanism is dominated by the electron-phonon coupling. This is again in good agreement with our data, where we observe deviations from the AD model setting in at temperatures below 120 K. Heid et al. have calculated the coupling strengths of the Bi<sub>2</sub>Se<sub>3</sub> CSSs to optical modes as a function of phonon energy [47]. They show that enhanced coupling occurs to phonons within an energy range of 17 to 22 meV with a reduced coupling for modes below 10 meV [47]. Even though Heid et al. state that the dominant coupling occurs via polar-type optical modes, significant coupling to Raman-active modes of the electron-

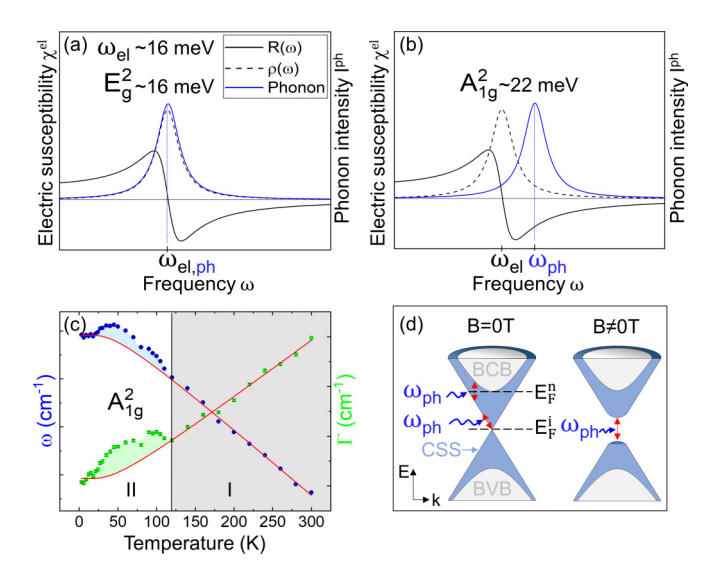


FIG. 3. (a),(b) The real  $R(\omega)$  and imaginary  $\rho(\omega)$  parts of the electric susceptibility are plotted together with the discrete state of a phonon modeled by a simple Lorentzian with a phonon frequency  $\omega_{\rm ph}$ . An overlap of both states is shown for the  $E_{\rm g}^2$  mode in (a) and the  $A_{\rm lg}^2$  mode in (b). (c) Temperature dependence of frequency and linewidth of the Bi<sub>2</sub>Se<sub>3</sub>  $A_{\rm lg}^2$  phonon. Two areas are indicated that account for different decay mechanisms of the phonon. (d) Schematic band structure of Bi<sub>2</sub>Se<sub>3</sub> with two possible locations of the Fermi level in an intrinsic  $(E_{\rm F}^i)$  and n-doped  $(E_{\rm F}^n)$  Bi<sub>2</sub>Se<sub>3</sub> nanoflake. The bulk conduction band (BCB) and bulk valence band (BVB) are labeled. Red arrows illustrate creations of electron-hole pairs by a Raman phonon  $\omega_{\rm ph}$ . The gapped Dirac cone is shown when a magnetic field  $B \neq 0$  T is applied.

phonon interaction is still present, as suggested in several studies [11,48]. Thus, our observations are in good agreement with the calculated coupling strengths, which support our findings for only very weak renormalizations in the  $A_{1g}^1$  mode at 9 meV and strong renormalizations in the  $E_{\rm g}^2$  (16.7 meV) and  $A_{1g}^2$  (21.9 meV) modes. The preceding analysis leads to the identification of two temperature regions with different dominant scattering mechanisms that are shown in Fig. 3(c). In region I, at higher temperatures, phonon-phonon coupling dominates the phonon decay by the anharmonic interaction and additional contributions from electron-phonon coupling are no longer evident. Therefore, we observe good agreement with the classic AD model in region I, where the bulk properties mask all surface-related effects. In region II, electronphonon coupling is significant and phonon renormalization can be observed when the surface contribution is high enough.

So far, we discussed the electron-phonon coupling from an energetic point of view. The  $A_{1g}^1$  phonon with an energy of around 9 meV should interfere with the electric susceptibility around 16 meV by coupling to the positive imaginary and real part. However, we do not observe electronic renormalizations for this mode. Hence, an additional aspect has to be considered that affects the coupling strength g between the phonons and the electric susceptibility. The eigenvectors of the phonons show significantly different displacement vectors for the  $A_{1g}^1$  phonon compared to the  $E_g^2$  and  $A_{1g}^2$  phonons.

The atomic displacements for the  $E_{\rm g}^2$  and  $A_{\rm lg}^2$  modes modulate the electric susceptibility related to the CSSs in the following way: For both modes, the partially negatively charged chalcogene (Se, Te) atoms terminating each QL vibrate opposite to the positively charged Bi atoms [18,49], whereas they vibrate in phase for the  $A_{\rm lg}^1$  mode. The electronic polarizability is, therefore, affected more strongly by the  $E_{\rm g}^2$  and  $A_{\rm lg}^2$  phonons, resulting in a stronger electron-phonon coupling and enhanced self-energy effects.

In a perfect single-crystalline Bi<sub>2</sub>Se<sub>3</sub> sample the Fermi level is expected to be located at the Dirac point [7], as indicated in Fig. 3(d). In this case, intracone electronic transitions in the upper Dirac cone are available. The electronphonon coupling strength increases linearly with the energy distance from the Dirac point due to the linear increase of the density of states expected for the 2D Dirac dispersion [47]. It is also possible that the Fermi level lies closer to the bulk conduction band due to inherent n doping that is often reported for naturally grown Bi<sub>2</sub>Se<sub>3</sub> [33] and is also shown in Fig. 3(d). In that case, transitions of the Dirac fermions into the bulk conduction band become possible and add to the intracone contributions. The coupling strength is expected to be enhanced when additional interband transitions are available [47], which explains our observed strong phonon renormalizations. We, therefore, expect the Fermi level in our Bi<sub>2</sub>Se<sub>3</sub> samples to lie within the bulk gap but closer to the bulk conduction bands.

The assumption of  $\chi^{el}$  being related to the CSSs is justified by two aspects. First, we were able to show the enhanced surface contributions of our flakes by the detection of IR modes up to high temperatures. Second, the electric susceptibility in the meV range can be associated with transitions involving Dirac cone states. Additional insight can be gained by manipulating the Dirac cone and the associated electric susceptibility by means of a magnetic field. Since the Dirac cone determines the low-energy electric susceptibility, its modification is also indicative of the presence of the CSSs. The changes in frequency and linewidth of the phonons as a function of magnetic field for  $Bi_2Se_3$  and  $Bi_2Te_3$  are shown in Figs. 4(a) to 4(f).

In agreement with our temperature dependent study and XPS results, we observe a magnetic field dependent renormalization of phonon energies and linewidths in Bi<sub>2</sub>Se<sub>3</sub>, but not in Bi<sub>2</sub>Te<sub>3</sub>. The absence of any phonon renormalization in Bi<sub>2</sub>Te<sub>3</sub> is again consistent with the reduced electronic density near the Fermi edge compared to the Bi<sub>2</sub>Se<sub>3</sub> sample. For Bi<sub>2</sub>Se<sub>3</sub>, however, magnetic field dependent self-energy corrections are observed in frequency and linewidth for the  $A_{1g}^2$  mode at 177 cm<sup>-1</sup>. At fields above 3 T, we find a simultaneous hardening and broadening of about 0.6 cm<sup>-1</sup> and 1.5 cm<sup>-1</sup>, respectively. Since it is known that in topological insulators a gap opening in the Dirac cone occurs in the presence of a magnetic field [23], our results point to a change in the electric susceptibility of the Dirac cone by the magnetic field. The change in the electric susceptibility would lead to a renormalization in the  $A_{1g}^2$  mode in Bi<sub>2</sub>Se<sub>3</sub>. A gap opening would shift and redistribute the electric susceptibility. The hardening and broadening of the  $A_{1g}^2$  mode with increasing field strengths indicate the coupling to an electric

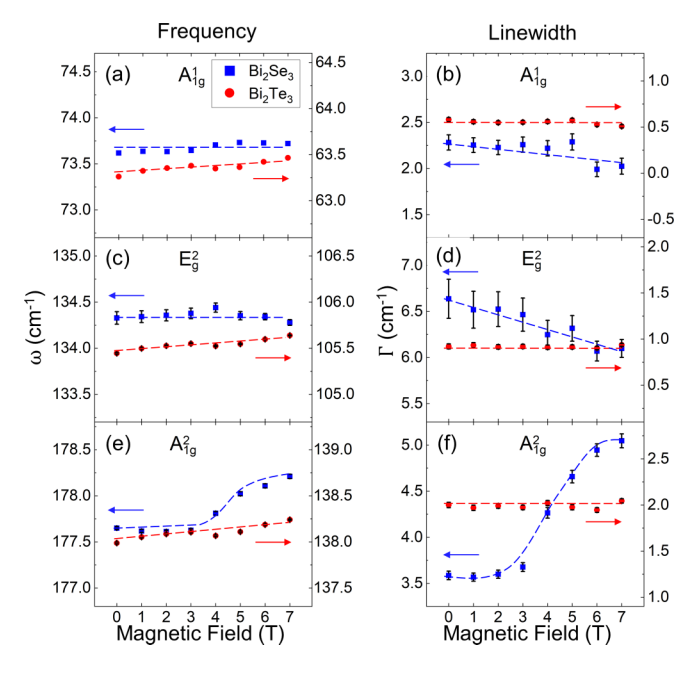


FIG. 4. Magnetic field dependent self-energy effects for Bi<sub>2</sub>Se<sub>3</sub> and Bi<sub>2</sub>Te<sub>3</sub> nanoflakes at 3 K in (*X*-)scattering geometry and Faraday configuration. The dependency of the three Raman modes in energy (left column) and linewidth (right column) with magnetic field is shown. All *y* axes are set to intervals of 2.0 cm<sup>-1</sup> for easier comparability. Bi<sub>2</sub>Te<sub>3</sub> phonons (red curves) show no significant change in energy and linewidth over the applied magnetic field range. For the Bi<sub>2</sub>Se<sub>3</sub> phonons (blue curves), clear changes in energy and linewidth can be observed for magnetic fields above 3 T. The dashed lines represent guides to the eye.

susceptibility with a lower energy than the phonon according to Eqs. (6) and (7). The decreasing linewidth of the  $E_{\rm g}^2$  mode, on the other hand, shows a reduced coupling to the electric susceptibility. We can therefore estimate the energy of a gap opening in the Dirac cone to be in the range of 16 to 22 meV, which would explain the phonon renormalizations. This finding is in agreement with results of Gooth *et al.* [50], who report a gap opening in the order of tens of meV by magnetic interactions in TI. According to our model, the phonons decay by coupling to interband transitions from the lower gapped Dirac cone to the upper one, as visualized in Fig. 3(d). The strong phonon self-energy corrections due to the electron-phonon interactions provide direct evidence

for the changes in the electric susceptibility in the CSSs at magnetic field strengths above 3 T.

### IV. CONCLUSION

In conclusion, we have investigated thin films of dropcasted Bi<sub>2</sub>Se<sub>3</sub> and Bi<sub>2</sub>Te<sub>3</sub> nanoflakes by means of temperature and magnetic field dependent Raman spectroscopy. The temperature dependence of the phonon dynamics in our Bi<sub>2</sub>Te<sub>3</sub> sample is readily described by the anharmonic phononphonon interaction, indicating a dominant bulk behavior. For Bi<sub>2</sub>Se<sub>3</sub>, we observe deviations from the AD model, which can be linked to additional contributions from the electronphonon interaction originating from the increased surface contribution. Our study suggests that the Dirac fermions contribute significantly to the electron-phonon interactions, which manifest in the strong phonon renormalizations in Bi<sub>2</sub>Se<sub>3</sub> at temperatures below 120 K. Additional magnetic field dependent Raman spectroscopy reveals strong phonon self-energy corrections in Bi<sub>2</sub>Se<sub>3</sub>, indicating the renormalization of the phonons by the continuum free carriers and a significant magnetoelectric coupling. The self-energy changes in the Bi<sub>2</sub>Se<sub>3</sub> phonons provide direct evidence for the manipulation of the CSSs by an applied magnetic field, which can be associated with a gap opening in the Dirac cone.

### ACKNOWLEDGMENTS

This work was funded by the Deutsche Forschungsgemeinschaft (DFG; German Research Foundation), DFG RU 773/8-1. Work at the University of Illinois was supported by the National Science Foundation under Grant No. NSF DMR 1800982. S.B., C.U., and M.R. would like to acknowledge the support from the Australian Research Council (ARC) through Grant No. DP170100415. The work at National University of Singapore is supported by the Ministry of Educations of Singapore AcRF Tier-2 (Grants No. MOE2017-T2-1-135, No. 323 MOE2018-T2-2-117, and No. MOE2018-T2-2-117), and Ministry of Education AcRF-1 (Grant No. R-144-000-423-114) and is acknowledged by the support of the Singapore Synchrotron Light Source (SSLS), which is a National Research Infrastructure under the National Research Foundation Singapore via NUS Core Support Grant No. C-380-003-003-001. We thank Robert Frömter and Dorota Koziej for the use of their scanning electron microscopes. We are further thankful for Robert Zierold and Stephan Martens for helpful discussions and magnetization measurements of our samples.

M. Z. Hasan and C. L. Kane, *Colloquium:* Topological insulators, Rev. Mod. Phys. 82, 3045 (2010).

<sup>[2]</sup> K. Von Klitzing, The quantized Hall effect, Rev. Mod. Phys. 58, 519 (1986).

<sup>[3]</sup> L. Fu, C. L. Kane, and E. J. Mele, Topological Insulators in Three Dimensions, Phys. Rev. Lett. 98, 106803 (2007).

<sup>[4]</sup> J. Betancourt, S. Li, X. Dang, J. Burton, E. Tsymbal, and J. Velev, Complex band structure of topological insulator Bi<sub>2</sub>Se<sub>3</sub>, J. Phys.: Condens. Matter 28, 395501 (2016).

<sup>[5]</sup> Y. Ando, Topological insulator materials, J. Phys. Soc. Jpn. 82, 102001 (2013).

<sup>[6]</sup> J. G. Analytis, J.-H. Chu, Y. Chen, F. Corredor, R. D. McDonald, Z. X. Shen, and I. R. Fisher, Bulk Fermi surface coexistence with Dirac surface state in Bi<sub>2</sub>Se<sub>3</sub>: A comparison of photoemission and Shubnikov–de Haas measurements, Phys. Rev. B 81, 205407 (2010).

<sup>[7]</sup> H. Zhang, C.-X. Liu, X.-L. Qi, X. Dai, Z. Fang, and S.-C. Zhang, Topological insulators in Bi<sub>2</sub>Se<sub>3</sub>, Bi<sub>2</sub>Te<sub>3</sub> and Sb<sub>2</sub>Te<sub>3</sub>

- with a single Dirac cone on the surface, Nat. Phys. 5, 438 (2009).
- [8] Y. Xia, D. Qian, D. Hsieh, L. Wray, A. Pal, H. Lin, A. Bansil, D. Grauer, Y. S. Hor, R. J. Cava, and M. Z. Hasan, Observation of a large-gap topological-insulator class with a single Dirac cone on the surface, Nat. Phys. 5, 398 (2009).
- [9] Y. L. Chen, J. G. Analytis, J.-H. Chu, Z. K. Liu, S.-K. Mo, X. L. Qi, H. J. Zhang, D. H. Lu, X. Dai, Z. Fang, S. C. Zhang, I. R. Fisher, Z. Hussain, and Z.-X. Shen, Experimental realization of a three-dimensional topological insulator, Bi<sub>2</sub>Te<sub>3</sub>, Science 325, 178 (2009).
- [10] D. Kim, Q. Li, P. Syers, N. P. Butch, J. Paglione, S. D. Sarma, and M. S. Fuhrer, Intrinsic Electron-Phonon Resistivity of Bi<sub>2</sub>Se<sub>3</sub> in the Topological Regime, Phys. Rev. Lett. 109, 166801 (2012).
- [11] C. Chen, Z. Xie, Y. Feng, H. Yi, A. Liang, S. He, D. Mou, J. He, Y. Peng, X. Liu *et al.*, Tunable Dirac fermion dynamics in topological insulators, Sci. Rep. 3, 2411 (2013).
- [12] M. Eddrief, P. Atkinson, V. Etgens, and B. Jusserand, Low-temperature Raman fingerprints for few-quintuple layer topological insulator Bi<sub>2</sub>Se<sub>3</sub> films epitaxied on GaAs, Nanotechnology 25, 245701 (2014).
- [13] S. Zhao, C. Beekman, L. Sandilands, J. Bashucky, D. Kwok, N. Lee, A. LaForge, S.-W. Cheong, and K. Burch, Fabrication and characterization of topological insulator Bi<sub>2</sub>Se<sub>3</sub> nanocrystals, Appl. Phys. Lett. 98, 141911 (2011).
- [14] K. Shahil, M. Hossain, V. Goyal, and A. Balandin, Micro-Raman spectroscopy of mechanically exfoliated few-quintuple layers of Bi<sub>2</sub>Te<sub>3</sub>, Bi<sub>2</sub>Se<sub>3</sub>, and Sb<sub>2</sub>Te<sub>3</sub> materials, J. Appl. Phys. 111, 054305 (2012).
- [15] V. Gnezdilov, Y. G. Pashkevich, H. Berger, E. Pomjakushina, K. Conder, and P. Lemmens, Helical fluctuations in the Raman response of the topological insulator Bi<sub>2</sub>Se<sub>3</sub>, Phys. Rev. B 84, 195118 (2011).
- [16] D. Teweldebrhan, V. Goyal, and A. A. Balandin, Exfoliation and characterization of bismuth telluride atomic quintuples and quasi-two-dimensional crystals, Nano Lett. 10, 1209 (2010).
- [17] K. M. F. Shahil, M. Hossain, D. Teweldebrhan, and A. Balandin, Crystal symmetry breaking in few-quintuple Bi<sub>2</sub>Te<sub>3</sub> films: Applications in nanometrology of topological insulators, Appl. Phys. Lett. **96**, 153103 (2010).
- [18] W. Richter, C. R. Becker, and H. Köhler, A Raman and farinfrared investigation of phonons in the rhombohedral V<sub>2</sub>-VI<sub>3</sub> compounds, Phys. Status Solidi (b) 84, 619 (1977).
- [19] B. Irfan, S. Sahoo, A. P. S. Gaur, M. Ahmadi, M. J.-F. Guinel, R. S. Katiyar, and R. Chatterjee, Temperature dependent Raman scattering studies of three dimensional topological insulators Bi<sub>2</sub>Se<sub>3</sub>, J. Appl. Phys. 115, 173506 (2014).
- [20] Y. Kim, X. Chen, Z. Wang, J. Shi, I. Miotkowski, Y. P. Chen, P. A. Sharma, A. L. Lima Sharma, M. A. Hekmaty, Z. Jiang, and D. Smirnov, Temperature dependence of Raman-active optical phonons in Bi<sub>2</sub>Se<sub>3</sub> and Sb<sub>2</sub>Te<sub>3</sub>, Appl. Phys. Lett. **100**, 071907 (2012).
- [21] F. Zhou, Y. Zhao, W. Zhou, and D. Tang, Temperature-dependent Raman scattering of large size hexagonal Bi<sub>2</sub>Se<sub>3</sub> single-crystal nanoplates, Appl. Sci. **8**, 1794 (2018).
- [22] D. Li, L. Li, D.-W. Liu, and J.-F. Li, Temperature dependence of the Raman spectra of Bi<sub>2</sub>Te<sub>3</sub> and Bi<sub>0.5</sub>Sb<sub>1.5</sub>Te<sub>3</sub> thermoelectric films, Phys. Status Solidi RRL **6**, 268 (2012).

- [23] X.-L. Qi, T. L. Hughes, and S.-C. Zhang, Topological field theory of time-reversal invariant insulators, Phys. Rev. B 78, 195424 (2008).
- [24] Y. Chen, J.-H. Chu, J. Analytis, Z. Liu, K. Igarashi, H.-H. Kuo, X. Qi, S.-K. Mo, R. Moore, D. Lu *et al.*, Massive Dirac fermion on the surface of a magnetically doped topological insulator, Science 329, 659 (2010).
- [25] P. Sessi, R. R. Biswas, T. Bathon, O. Storz, S. Wilfert, A. Barla, K. A. Kokh, O. E. Tereshchenko, K. Fauth, M. Bode *et al.*, Dual nature of magnetic dopants and competing trends in topological insulators, Nat. Commun. 7, 12027 (2016).
- [26] W. Luo and X.-L. Qi, Massive Dirac surface states in topological insulator/magnetic insulator heterostructures, Phys. Rev. B 87, 085431 (2013).
- [27] P. Wei, F. Katmis, B. A. Assaf, H. Steinberg, P. Jarillo-Herrero, D. Heiman, and J. S. Moodera, Exchange-Coupling-Induced Symmetry Breaking in Topological Insulators, Phys. Rev. Lett. 110, 186807 (2013).
- [28] S. Buchenau, P. Sergelius, C. Wiegand, R. Zierold, H. S. Shin, M. Rübhausen, J. Gooth, K. Nielsch *et al.*, Symmetry breaking of the surface mediated quantum Hall effect in Bi<sub>2</sub>Se<sub>3</sub> nanoplates using Fe<sub>3</sub>O<sub>4</sub> substrates, 2D Mater. 4, 015044 (2017).
- [29] D. Biswas, S. Thakur, K. Ali, G. Balakrishnan, and K. Maiti, Anomalies of a topologically ordered surface, Sci. Rep. 5, 10260 (2015).
- [30] S. Buchenau, L. O. Akinsinde, M. Zocher, D. Rukser, U. Schürmann, L. Kienle, B. Grimm-Lebsanft, and M. Rübhausen, Scalable polyol synthesis for few quintuple layer thin and ultra high aspect ratio Bi<sub>2</sub>Se<sub>3</sub> structures, Solid State Commun. 281, 49 (2018).
- [31] Y. Zhang, L. P. Hu, T. J. Zhu, J. Xie, and X. B. Zhao, High yield Bi<sub>2</sub>Te<sub>3</sub> single crystal nanosheets with uniform morphology via a solvothermal synthesis, Crystal Growth Des. **13**, 645 (2013).
- [32] See Supplemental Material at http://link.aps.org/supplemental/ 10.1103/PhysRevB.101.245431 for details of the nanoflake synthesis and characterization, additional Raman measurements, and *n*-doping study of the Bi<sub>2</sub>Se<sub>3</sub> nanoflakes.
- [33] Y. Zhang, K. He, C.-Z. Chang, C.-L. Song, L.-L. Wang, X. Chen, J.-F. Jia, Z. Fang, X. Dai, W.-Y. Shan, S.-Q. Shen, Q. Niu, X.-L. Qi, S.-C. Zhang, X.-C. Ma, and Q.-K. Xue, Crossover of the three-dimensional topological insulator Bi<sub>2</sub>Se<sub>3</sub> to the two-dimensional limit, Nat. Phys. 6, 584 (2010).
- [34] H. M. Benia, C. Lin, K. Kern, and C. R. Ast, Reactive Chemical Doping of the Bi<sub>2</sub>Se<sub>3</sub> Topological Insulator, Phys. Rev. Lett. **107**, 177602 (2011).
- [35] D. Kong, J. J. Cha, K. Lai, H. Peng, J. G. Analytis, S. Meister, Y. Chen, H.-J. Zhang, I. R. Fisher, Z.-X. Shen *et al.*, Rapid surface oxidation as a source of surface degradation factor for Bi<sub>2</sub>Se<sub>3</sub>, ACS Nano 5, 4698 (2011).
- [36] B. Yan, D. Zhang, and C. Felser, Topological surface states of Bi<sub>2</sub>Se<sub>3</sub> coexisting with Se vacancies, Phys. Status Solidi RRL 7, 148 (2013).
- [37] B. Schulz, J. Bäckström, D. Budelmann, R. Maeser, M. Rübhausen, M. V. Klein, E. Schoeffel, A. Mihill, and S. Yoon, Fully reflective deep ultraviolet to near infrared spectrometer and entrance optics for resonance Raman spectroscopy, Rev. Sci. Instrum. 76, 073107 (2005).

- [38] C. Arguello, D. L. Rousseau, and S. P. d. S. Porto, First-order Raman effect in wurtzite-type crystals, Phys. Rev. **181**, 1351 (1969).
- [39] J. Zhang, Z. Peng, A. Soni, Y. Zhao, Y. Xiong, B. Peng, J. Wang, M. S. Dresselhaus, and Q. Xiong, Raman spectroscopy of few-quintuple layer topological insulator Bi<sub>2</sub>Se<sub>3</sub> nanoplatelets, Nano Lett. 11, 2407 (2011).
- [40] Y. Liang, W. Wang, B. Zeng, G. Zhang, J. Huang, J. Li, T. Li, Y. Song, and X. Zhang, Raman scattering investigation of Bi<sub>2</sub>Te<sub>3</sub> hexagonal nanoplates prepared by a solvothermal process in the absence of naoh, J. Alloys Compd. **509**, 5147 (2011).
- [41] R. He, Z. Wang, R. L. J. Qiu, C. Delaney, B. Beck, T. E. Kidd, C. C. Chancey, and X. P. A. Gao, Observation of infraredactive modes in Raman scattering from topological insulator nanoplates, Nanotechnology 23, 455703 (2012).
- [42] P. G. Klemens, Anharmonic decay of optical phonons, Phys. Rev. 148, 845 (1966).
- [43] N. Bonini, M. Lazzeri, N. Marzari, and F. Mauri, Phonon Anharmonicities in Graphite and Graphene, Phys. Rev. Lett. 99, 176802 (2007).
- [44] E. H. Hasdeo, A. R. T. Nugraha, M. S. Dresselhaus, and R. Saito, Breit-Wigner-Fano line shapes in

- Raman spectra of graphene, Phys. Rev. B **90**, 245140 (2014).
- [45] M. A. Rübhausen, Electronic correlations in cuprate superconductors - An inelastic light scattering study, Ph.D. thesis, Universität Hamburg, 1998.
- [46] M. Cardona, *Light Scattering in Solids I Introductory Concepts*, edited by M. Cardona (Springer-Verlag, Berlin, 1983).
- [47] R. Heid, I. Yu. Sklyadneva, and E. V. Chulkov, Electron-phonon coupling in topological surface states: The role of polar optical modes, Sci. Rep. **7**, 1095 (2017).
- [48] T. Kondo, Y. Nakashima, Y. Ota, Y. Ishida, W. Malaeb, K. Okazaki, S. Shin, M. Kriener, S. Sasaki, K. Segawa *et al.*, Anomalous Dressing of Dirac Fermions in the Topological Surface State of Bi<sub>2</sub>Se<sub>3</sub>, Bi<sub>2</sub>Te<sub>3</sub>, and Cu-Doped Bi<sub>2</sub>Se<sub>3</sub>, Phys. Rev. Lett. 110, 217601 (2013).
- [49] S. Mishra, S. Satpathy, and O. Jepsen, Electronic structure and thermoelectric properties of bismuth telluride and bismuth selenide, J. Phys.: Condens. Matter 9, 461 (1997).
- [50] J. Gooth, R. Zierold, P. Sergelius, B. Hamdou, J. Garcia, C. Damm, B. Rellinghaus, H. J. Pettersson, A. Pertsova, C. Canali et al., Local magnetic suppression of topological surface states in Bi<sub>2</sub>Te<sub>3</sub> nanowires, ACS Nano 10, 7180 (2016).